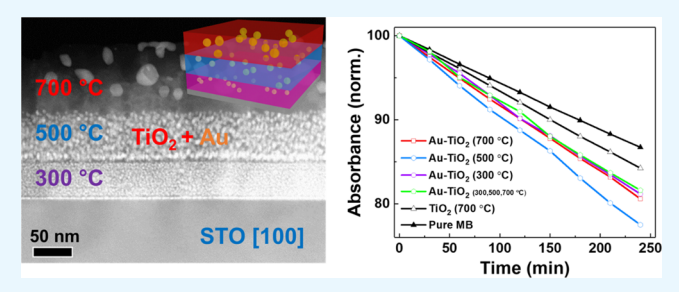


# Tailorable Au Nanoparticles Embedded in Epitaxial TiO<sub>2</sub> Thin Films for Tunable Optical Properties

Shikhar Misra,<sup>†</sup> Leigang Li,<sup>†</sup> Jie Jian,<sup>†</sup> Jijie Huang,<sup>†</sup> Xuejing Wang,<sup>†</sup> Dmitry Zemlyanov,<sup>§</sup> Ji-Wook Jang,<sup>⊥</sup> Fabio H. Ribeiro, I and Haiyan Wang\*, I and Haiyan Wang\*, I are the state of the s

Supporting Information

ABSTRACT: The unique property of plasmonic materials to localize light into deep sub-wavelength regime has greatly driven various applications in the field of photovoltaics, sensors, and photocatalysis. Here, we demonstrate the onestep growth of an oxide-metal hybrid thin film incorporating well-dispersed gold (Au) nanoparticles (NPs) with tailorable particle shape and diameters (ranging from 2 to 20 nm) embedded in highly epitaxial TiO2 matrix, deposited using pulsed laser deposition. Incorporation of Au NPs reduces the band gap of TiO2 and enhances light absorption in the visible



regime owing to the excitation of localized surface plasmons. Optical properties, including the plasmonic response and permittivity, and photocatalytic activities of the Au-TiO2 hybrid materials are effectively tuned as a function of the Au NP sizes. Such optical property tuning is well captured using full-field simulations and the effective medium theory for better understanding of the physical phenomena. The tailorable shape and size of Au NPs embedded in TiO2 matrix present a novel oxide-metal hybrid material platform for optical property tuning and highly efficient plasmonic properties for future oxidebased photocatalytic sensors and devices.

KEYWORDS: TiO2, Au (gold) nanoparticles, oxide-metal hybrid materials, plasmonics, optical property tuning

#### INTRODUCTION

Titanium dioxide (TiO<sub>2</sub>), a wide band gap semiconductor (~3 eV for rutile and ~3.2 eV for anatase), has been extensively studied for its photocatalytic properties following the discovery of the Fujishima-Honda effect in 1972. Since this discovery, TiO<sub>2</sub> has been proposed to be used in the areas of solar cells, water-splitting, degradation of pollutants and organic molecules, water purification, etc.<sup>2-5</sup> Toward the practical applications of TiO2 as photocatalyst, its wide band gap has limited the usage in the ultraviolet regime, which constitutes ~5% of the solar electromagnetic spectrum. Much efforts have been devoted to increase its efficiency in the visible regime by incorporating plasmonic nanostructures in TiO2.7-11 For example, the integration of noble-metal nanoparticles (NPs) in a semiconductor has attracted much attention because of the strong absorption of light in the visible regime due to the resonant oscillation of surface conduction electrons excited by light, known as localized surface plasmon resonance (SPR). The SPR effect has been efficiently exploited in various applications, such as photocatalysis and photovoltaics. 12,13

To further enhance the absorption efficiency of solar spectrum, noble-metal-based plasmonic structures can be further nanoengineered to achieve extreme control over light at nanoscale. For example, plasmonic structures have the ability to enhance low-intensity light by concentrating light over a small area. More recent applications of nanoscale plasmonic materials are in quantum optics, cloaks, water purification, solar distillation, and reconfigurable metamaterials. 14-18 Among all plasmonic materials, Au is one of the most promising and widely used materials because of its biocompatibility, high stability, and excellent quality factor.<sup>15</sup> allows the nanocomposite structure to harvest sub-band gap photons, thus increasing its absorption range.

Most of the metal integrations focus on surface incorporation by various methods such as evaporation, 7,20,21 photocatalytic reduction,<sup>8</sup> chemical reduction,<sup>22</sup> colloid photodeposition,<sup>23</sup> and facile adsorption.<sup>24</sup> Incorporating the metal nanostructures within an oxide matrix poses significant challenges due to potential interdiffusion, oxidation, and structure instability. For example, most of the metals readily diffuse in oxide matrix. Very recently, several successful demonstrations on the growth of epitaxial metal-oxide

Received: July 19, 2018 Accepted: August 29, 2018 Published: August 29, 2018



<sup>&</sup>lt;sup>†</sup>School of Materials Engineering, <sup>‡</sup>School of Electrical and Computer Engineering, <sup>§</sup>Birck Nanotechnology Center, and <sup>||</sup>School of Chemical Engineering, Purdue University, West Lafayette, Indiana 47907, United States

 $<sup>^\</sup>perp$ Department of Energy and Chemical Engineering, Ulsan National Institute of Science and Technology (UNIST), Ulsan 44919, South Korea

**ACS Applied Materials & Interfaces** 

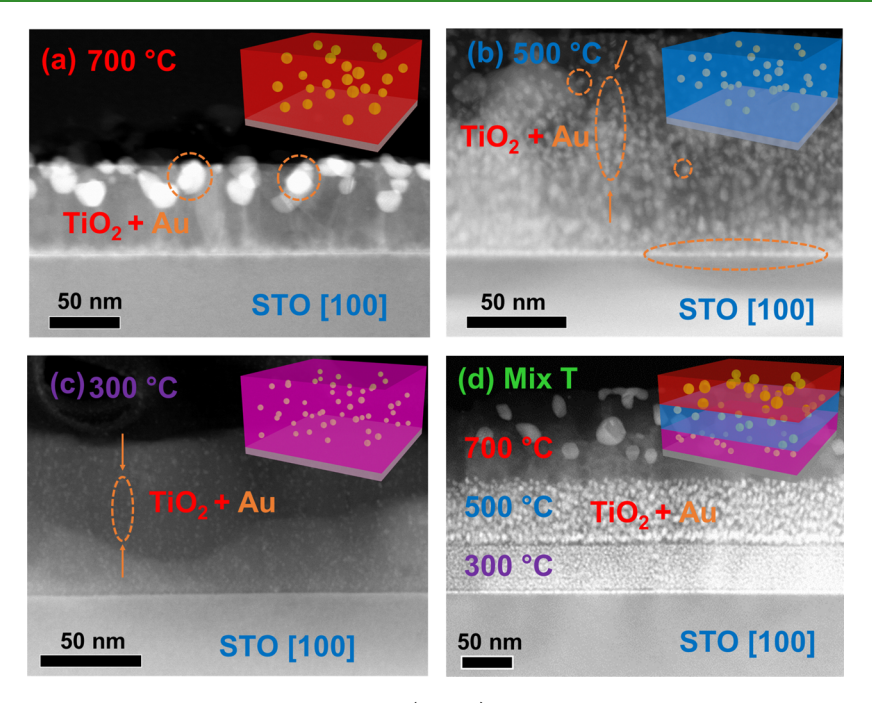


Figure 1. Cross-sectional scanning transmission electron microscopy (STEM) images showing Au NPs embedded in epitaxial TiO<sub>2</sub> thin film for growth temperature of (a) 700 °C, (b) 500 °C, (c) 300 °C, and (d) mixed temperature.

systems have opened the possibilities of such hybrid material platform with the two phases deposited simultaneously using pulsed laser deposition (PLD).<sup>2,5-2,7</sup>

In this work, we fabricated a new nanostructure with Au NPs embedded in TiO<sub>2</sub> matrix grown on STO(001) using PLD, as illustrated in the embedded schematics in Figure 1. The advantages of PLD include good stoichiometry control, flexibility in co-growing two-phase nanocomposites, and relatively low contamination levels.<sup>28–30</sup> Moreover, being a nonequilibrium process, PLD is effective in fabricating thin films with complex stoichiometry and producing metastable phases such as anatase phase (instead of the bulk thermodynamically stable rutile phase), which has been reported as a better photocatalyst than rutile.<sup>31</sup> However, very limited studies have been conducted regarding plasmonic noble-metal NPs embedded in photocatalysts using PLD and are mostly based on nanocrystalline  ${\rm TiO_2}$  thin films.  $^{\rm 32,33}$  Here, we demonstrate the ability to incorporate Au nanoparticles uniformly and epitaxially in TiO2 matrix. More interestingly, the size, shape, and distribution of Au NPs can be effectively tailored to tune the plasmonic properties of the Au NPs and the photocatalytic properties of TiO2. This straightforward approach is demonstrated by fabricating a multilayer stack of Au-TiO<sub>2</sub> with distinct sizes of Au NPs by varying the substrate temperature. In addition, effective medium approximation (EMA) coupled with spectroscopic ellipsometry can be used to estimate the Au NP size effect on the effective permittivity of Au-TiO<sub>2</sub> nanocomposite.

# ■ RESULTS AND DISCUSSION

To study the deposition temperature effect on the size and shape dependence of Au NPs embedded in  ${\rm TiO_2}$ , high-angle annular dark-field scanning transmission electron microscopy (HAADF-STEM) studies were performed on all samples deposited at 300, 500, and 700 °C and three mixed temperatures. Figures 1 and S1 (in the Supporting Information) show the cross-sectional STEM images of  ${\rm TiO_2}$ 

and Au-TiO<sub>2</sub> thin films on STO(001) and MgO(001), respectively. The STEM imaging under HAADF condition is also called Z-contrast where the image contrast is roughly proportional to Z<sup>2,34</sup> Such composition-based contrast difference in STEM is ideal for microstructural analysis of two-phase nanocomposites. STEM image clearly shows the Au NPs uniformly embedded in TiO2 matrix where Au has a brighter contrast than that of TiO<sub>2</sub> because of its higher atomic number (Z) (Figure 1). The average Au NP size decreases as the substrate temperature reduces. The average Au NP size decreases from ~17 nm at 700 °C to ~5 nm at 500 °C and  $\sim$ 2 nm at 300 °C. The same trend is also observed for the samples on MgO(001) substrates (Figure S1), i.e., the particle size decreases from ~9 nm at 700 °C to ~4 nm at 500 °C and ~2 nm at 300 °C. Higher growth temperature increases the surface mobility (i.e., surface diffusivity) of the Au ad-atoms, which leads to larger Au growth islands, e.g., larger Au nanoparticles in the TiO2 matrix for the case of the 700 °C sample. In comparison, decreasing the temperature to 500 and 300 °C decreases the surface mobility of Au NPs and thus leads to smaller Au NP formation. Interestingly, the particle shape also changes with the deposition temperature to minimize the overall interfacial energy. At 700 °C, well-faceted large Au nanoparticles are observed. The particle shape changes to elliptical and spherical for samples deposited at 500 and 300 °C, respectively, and the particles show more uniform distribution in the matrix for both cases. Figure 1d shows the film grown at three different temperatures consequently, which clearly illustrates the ability to easily tune the sizes and distribution of Au NPs via the deposition temperature control. Another notable feature observed in the STEM images is the ability of the Au NPs to self-align to form pillars. At 500 °C, the tendency to form nanopillar-like structures from the vertically aligned nanoparticles is clear, as indicated by the circled areas. The ability of Au particles to align as nanopillars suggests the possible strain-driven alignment of Au NPs in TiO2 matrix. Overall, the growth

temperature plays a critical role in determining the particle shape and size. For all samples, a seed layer of Au NPs is nucleated near the film-substrate interface to assist the initial nucleation and growth of the Au-TiO2 nanocomposite structure.

The X-ray diffraction (XRD)  $\theta$ –2 $\theta$  scans of TiO<sub>2</sub> films (Figure S3) confirm the highly textured growth of anatase TiO<sub>2</sub> along (004) direction for all cases. As opposed to the more thermodynamically stable rutile phase, the growth of metastable anatase phase results in the lowering of the overall free energy by forming a semicoherent interface and is the preferred phase to form on STO because of better epitaxial matching.<sup>35</sup> Au peaks show the presence of two major orientations of (002) and (111), and the orientation preference varies as a function of temperature, i.e., (002) for the 700 °C one and (111) for the 500 °C one and the 3temperature one. A narrow full-width half maximum of the rocking curve for the (004) TiO<sub>2</sub> peak indicates the high epitaxial and crystalline quality of the film (Figure S4), whereas the TiO<sub>2</sub> peak completely disappears for the 300 °C sample, implying that the crystallinity of the film reduces at lower growth temperatures. Moreover, the XRD  $\theta$ – $2\theta$  scans (Figure S3) and the selected area electron diffraction (SAED) pattern (Figure S2) confirm the epitaxial growth of TiO<sub>2</sub> and Au NPs on STO evidenced by their distinguished diffraction dots. The growth orientations of TiO2 and Au are determined to be  $Au(002)//TiO_2(004)//STO(002)$  and Au(200)// $TiO_2(200)//STO(200)$ . Hence, the growth temperature plays a critical role in determining the film crystallinity and the Au NP sizes.

An important characteristic of the Au-TiO<sub>2</sub> nanocomposite thin films is their highly tunable optical properties. The optical response of nanocomposites varies greatly with the Au NPs' size, shape, and density. All films on MgO substrates were characterized by optical transmittance measurements at the normal incident angle. Figure 2a shows the UV-vis-nearinfrared (NIR) transmittance spectra of the films grown at different temperatures. First, all samples present an obvious absorption edge around 350 nm that is related to the band gap of the TiO<sub>2</sub> films. Specifically, the absorption edge of TiO<sub>2</sub> presents an obvious redshift from 380 nm (pure TiO<sub>2</sub>) to as high as 460 nm (grown at mix temperature) in the visible regime because of the presence of Au NPs. A detailed band gap calculation using the Tauc plot yields the plot in Figure 2b where the band gap of TiO<sub>2</sub> varies from 3.25 eV (grown at 700 °C, closer to its bulk value of 3.2 eV) to 2.91 eV (grown at 300 °C). Such obvious  $E_{\sigma}$  reduction is attributed to possible TiO<sub>2</sub> film stoichiometry variation due to the Au inclusions as well as the interface effects at the Au-TiO2 interfaces, which will be discussed in more detail later. It has been reported that the variation in oxygen stoichiometry could change the conduction band of oxide semiconductors and thus lead to the band gap variation.<sup>36,37</sup> In this work, we have confirmed that the Au NP incorporation actually results in more stoichiometric TiO2 (Ti/O ratio of 1:2) using X-ray photoelectron spectroscopy (XPS) analysis and considered this as one of the possible reasons for the band gap tuning. In addition, interface-based strain tuning could also cause tuning in bandgaps, as shown by others.<sup>38</sup> Second, all Au-TiO<sub>2</sub> nanocomposite films present an obvious plasmonic absorption peak and the peak position shifts systematically. We recall that the Au NPs' size varies from ~17 nm (700 °C) to 2 nm (300 °C). Such large tunability in Au NP size results in the large shift in the plasmonic absorption

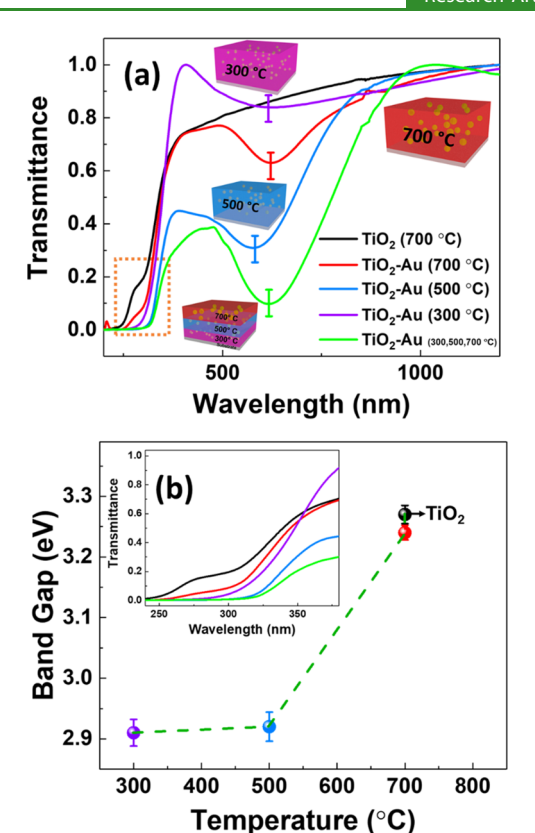


Figure 2. (a) Transmittance spectra of the TiO<sub>2</sub> and Au-TiO<sub>2</sub> nanocomposite films for varied growth temperature and (b) their corresponding band gap calculated using the Tauc plot. The marked region in (a) is shown as an inset in (b).

peak from 578 nm (500 °C sample) to 622 nm (700 °C sample). Note that the plasmonic absorption for the sample grown at 300 °C is relatively weak and broad and thus there is no clear SPR peak assigned. More interestingly, the film grown under the mixed temperatures of 300, 500, and 700 °C shows the maximum absorption of light over a very broad range of spectrum from ~1000 to 480 nm, which is attributed to the various Au NP sizes introduced by the three different growth temperatures. Such systematic SPR peak shifting for the Au-TiO<sub>2</sub> samples is believed to be related to the tunable Au NP sizes, which leads to the enhanced plasmonic absorption at specific wavelengths.

Furthermore, the anisotropic optical properties of the Au-TiO<sub>2</sub> film deposited under mixed temperatures have been explored using angular-dependent transmittance measurements. A schematic of the setup is shown in Figure S5a. The incident depolarized light strikes the sample at various incidence angles, and the subsequent transmission is recorded. Figure S5 summarizes the angular-dependent transmittance and reflectivity results of samples grown at mixed temperatures. The plasmonic resonance peak shows a redshift from 579 to 592 nm as the incident angle decreases, which is due to the anisotropic nature of Au NPs (see Figure S6b). At higher angles, the light in higher wavelength regime is required for the plasmonic resonance of Au NPs. Moreover, varying the transmittance angle from 20 to  $-20^{\circ}$  increases the absorption by 3% (Figure S5c). Hence, angular measurement provides a direct measure of the anisotropy nature in the material and confirms the shape dependence of the plasmonic response. It is observed that transmittance decreases at higher angles in all **ACS Applied Materials & Interfaces** 

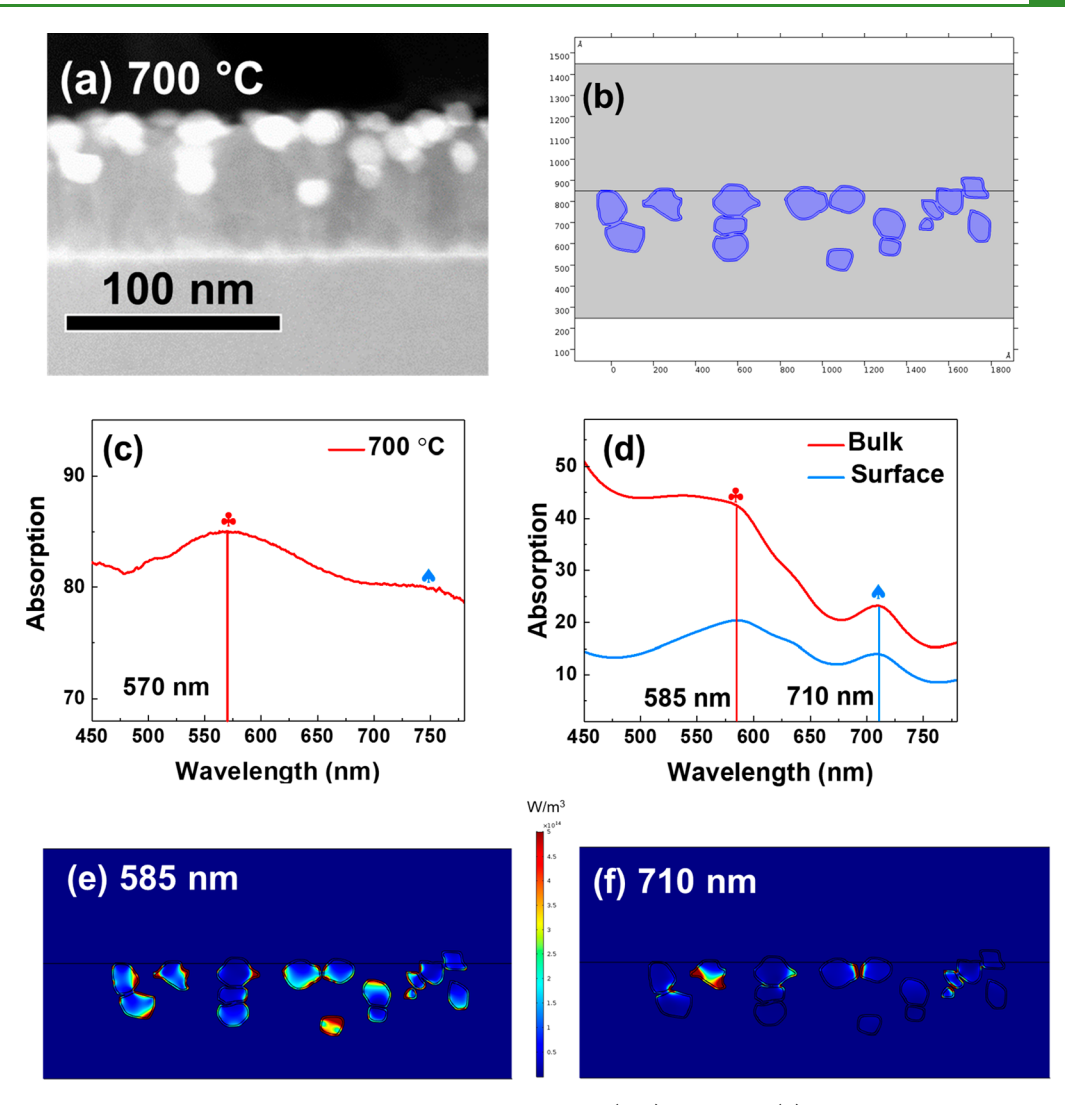


Figure 3. (a) Cross-sectional STEM image of the  $Au-TiO_2$  film grown on STO(001) at 700 °C, (b) approximate geometry used to simulate the absorption spectra, (c) experimental absorption spectra and (d) calculated absorption spectra showing the surface and bulk contribution of Au NPs, (e) absorption map corresponding to incident illumination at 585 nm and (f) 710 nm.

samples. This is because at higher angles, the incident and reflected wave can destructively interfere more easily, thus decreasing the transmission (and increasing the reflection).

To gain a better understanding of the optical properties, the optical response in the nanocomposite system was modeled using COMSOL Multiphysics 5.3. Figure 3a shows the crosssectional STEM image of Au-TiO<sub>2</sub> sample grown at 700 °C, which was used to approximate the simulated geometry shown in Figure 3b. Experimental and calculated absorption spectra show a reasonable match, as shown in Figure 3c,d, respectively. The absorption spectra show two major peaks at regimes near 580 and 710 nm, observed in both simulated and experimental spectra. Figure 3e,f maps the absorption of Au NPs at 585 and 710 nm, respectively. On the basis of the calculation, it is observed that the peak near 580 nm is caused by Au NPs themselves whereas the peak near 710 nm corresponds to the sharp corners and interparticle coupling of Au NPs. Figure 3d shows the absorption (W/m) in Au NPs from the surface of Au NPs and from the bulk Au NPs. It again shows that the surface (coupling) effect becomes more prominent at higher wavelengths as the bulk absorption decreases at higher wavelengths. The difference between the experimental and

simulation spectrum could be because the simulation was based on the geometry from a small region whereas the experimental data was collected from a large area of the samples.

Au NPs introduced during the growth of TiO2 thin films have major impact on the overall optical response of the hybrid materials. One of the possible reasons for such strong effects is the possible impact on the overall stoichiometry of TiO<sub>2</sub> matrix. Thus, a detailed study on the film composition and oxidation states of the elements were studied using XPS. Survey spectra showed the presence of Ti, Au, O, and C. Highresolution XPS spectra of Ti 2p and Au 4f core levels for pure TiO2 grown at 700 °C and Au-TiO2 films grown at 300 and 700 °C are shown in Figure 4. The Ti 2p<sub>3/2</sub> and Ti 2p<sub>1/2</sub> peaks have binding energies of 458.5 and 464.3 eV, respectively, with a spin-orbital splitting of 5.8 eV. According to the Ti 2p peak positions, Ti chemical state can be unambiguously assigned to Ti<sup>4+</sup> state: these values are consistent with those reported for  ${\rm TiO_2~films.}^{33,39}$  The Au  ${\rm 4f_{7/2}}$  and Au  ${\rm 4f_{5/2}}$  peaks have binding energies of approximately 84.1 and 87.8 eV, respectively, at 300 °C with a spin-orbital splitting of 3.7 eV. The Au 4f peak position and shape correspond to the metallic gold Au<sup>0</sup>. The

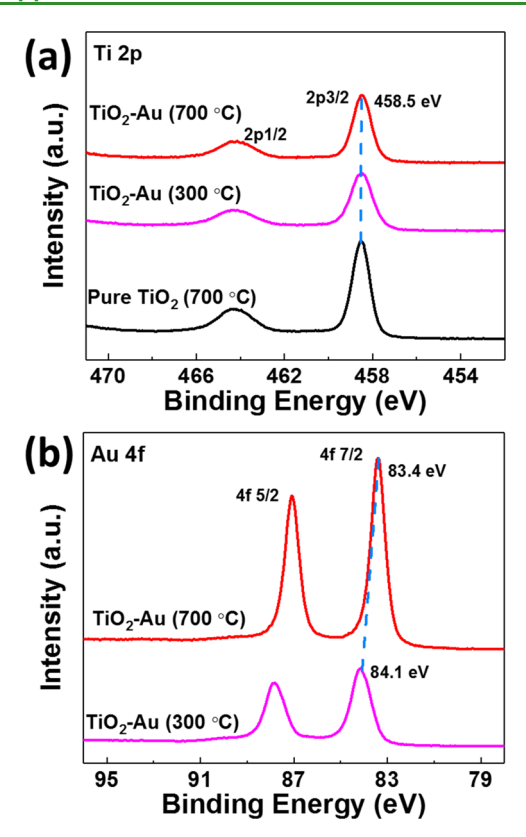


Figure 4. High-resolution XPS spectra of (a) Ti 2p and (b) Au 4f of Au-TiO2 nanocomposite thin film.

low binding energy shift of the Au 4f<sub>7/2</sub> peak from 84.1 to 83.4 eV is observed as the growth temperature increases from 300 to 700 °C. This shift can be explained by the charge transfer from titania to Au NPs.8 Interestingly, the interfacial charge transfer in the case of Au-TiO<sub>2</sub> sample grown at 700 °C is more than that of the sample grown at 300 °C. The binding energy of Au increases with the decreasing particle size. Atomic percentage calculated on the basis of the XPS results shows that TiO<sub>2</sub>-Au has a closer stoichiometric ratio (atomic ratio of Ti/O) of 1:2.

Tunability of the optical properties with and without Au addition was evaluated on the basis of the spectroscopic ellipsometry measurement. The data fittings were performed assuming isotropic response  $(\varepsilon_{[001]} = \varepsilon_{[010]} = \varepsilon_{[100]})$  through the use of general oscillator models to enforce the Kramers-Kronig consistency. Figure 5a shows the ellipsometer parameter  $\psi$  fitted using an appropriate model to calculate the dielectric permittivity (see Methods section). The dielectric complex function, i.e., permittivity real part  $\varepsilon'$  and imaginary part  $\varepsilon''$  of the TiO<sub>2</sub> and Au-TiO<sub>2</sub> nanocomposite are plotted in Figure 5b. The optical constants calculated from Maxwell Garnett EMA (see the Supporting Information) closely match with the constants obtained by the ellipsometry model fitting shown in Figure 5b. The additional broadening may be due to anisotropic nature or the size variation of the Au NPs. It is interesting to note that the permittivity of TiO<sub>2</sub> sample deposited at 300 °C is the same as that of the TiO<sub>2</sub> sample deposited at 700 °C. Therefore, significant effects on tuning the overall permittivity of the Au-TiO<sub>2</sub> nanocomposite comes primarily from the Au NPs and the TiO2 crystallinity plays a minor role in tailoring the properties. The effects of the Au NPs on the overall TiO<sub>2</sub> photocatalytic properties were

further characterized by photodegradation of methylene blue (MB) dye with an initial concentration of 10 mg/L. Figure 5c shows a typical measurement of MB degradation over time. The normalized absorbance of pure MB, pure TiO<sub>2</sub>, and Au-TiO<sub>2</sub> grown at 300, 500, and 700 °C and mix temperature is plotted in Figure 5d. Interestingly, the experimental results demonstrate that the Au-TiO2 grown at 500 °C has the highest photodegradation rate among all five samples. The increased photoactivity of the 500 °C sample can be attributed to the lower band gap of TiO2 ~2.9 eV (see Figure 2b) and higher plasmonic absorption over a broader wavelength range as compared to those of the 300 and 700 °C sample (see Figure 2a). Thus, these results directly correlate the size dependence of Au NPs with their photocatalytic activity and demonstrate potential in designing photocatalytic devices with higher efficiencies. Different Au NP sizes have resulted in the obvious tuning of the absorption peak and the band gap of TiO<sub>2</sub>, as shown earlier. Therefore, we believe that the obvious tuning effects on permittivity and catalytic properties observed in the Au-TiO2 samples come primarily from the Au NPs'

There are several key features that this novel structure provides over other previously reported  $Au-TiO_2$  systems.  $^{7,9,20,40-42}$  First, the fully embedded Au NPs inside the TiO<sub>2</sub> matrix present efficient charge transfer to the semiconductor matrix as compared to other surface Au NP cases.<sup>21</sup> This is attributed to the increased interfacial area available for electron injection. Second, the shape, size, and density of Au NPs can be tailored and achieved by using a one-step growth method. Controlling the shape and size of NPs is important for tailoring their plasmonic response and for further exploring the size dependence on charge injection efficiency.<sup>21</sup> A highly uniform size distribution of Au NPs can also be achieved. In addition, very small Au NPs, as fine as 2 nm, can be achieved, which is much less than the mean free path of electronelectron scattering (~30 nm for a 2 eV electron) and ideal for the electron to reach the interface. Third, the optical permittivity and catalytic properties of the Au-TiO2 nanocomposites can be effectively tuned by varying the Au NP size, as measured using ellipsometry and photodegradation experiments. Fourth, the co-growth method provides flexibility in morphology control (in terms of crystallinity, purity, and composition) over other methods previously employed to fabricate  $Au-TiO_2$  nanocomposites. <sup>32,33</sup> It is possible to adopt this approach for incorporating other plasmonic nanostructures in oxide matrix for enhanced optical, electrochemical, and photocatalytic properties. Incorporation of Au particles increases the solar energy harvesting range to as high as 1000 nm (compared to that of bare TiO2, which is active below 390 nm), allowing applications such as photocatalysis and light concentrators. 43 The one-step PLD process employed here offers easy control of the volume fraction of Au NPs, which provides new opportunities to manipulate light-matter interaction over a wide range of wavelengths.

# CONCLUSIONS

In summary, we have demonstrated a one-step PLD deposition technique to deposit highly textured metastable anatase TiO<sub>2</sub>-Au nanocomposite thin films with highly tailorable shape and size of Au NPs by varying the growth temperature. Incorporation of Au NPs effectively tunes the band gap of TiO2. The shape and size tuning of Au NPs increases the absorption efficiency over a broad optical spectrum. The

**ACS Applied Materials & Interfaces** 

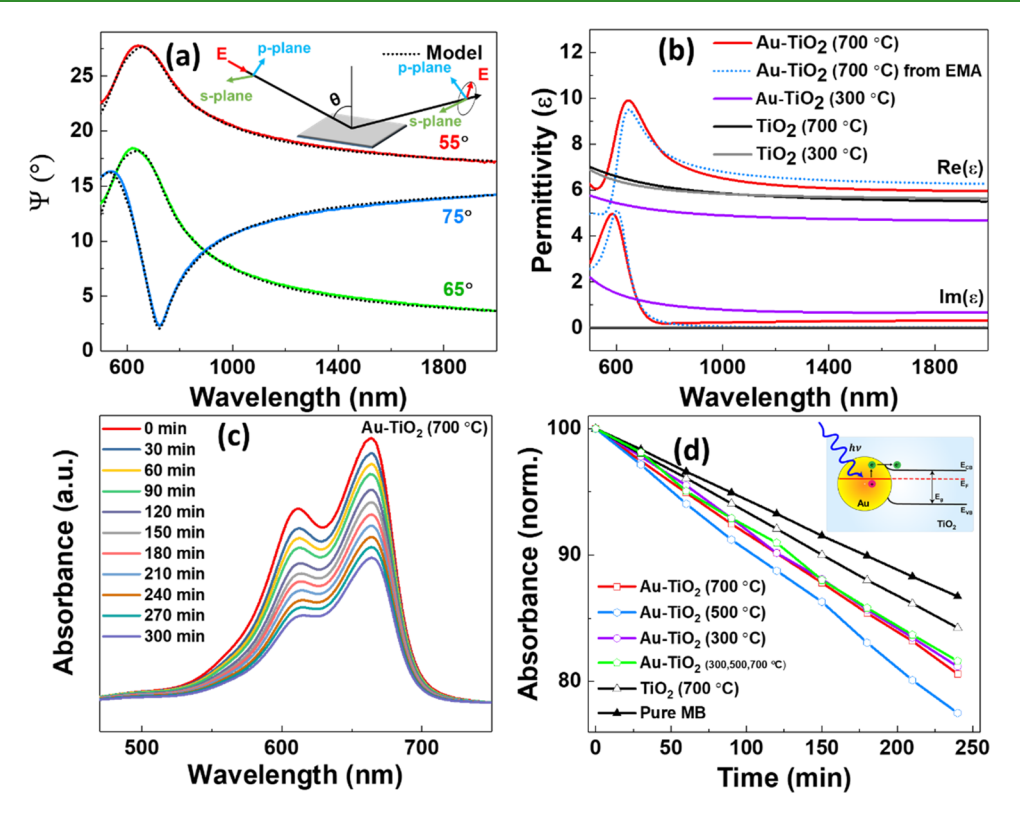


Figure 5. (a) Experimental (solid) and fitted (dot) components of the ellipsometric parameter  $\psi$  for the TiO<sub>2</sub>-Au sample deposited at 700 °C. Inset shows the ellipsometer measurement setup. The ellipsometer parameters  $\psi$  and  $\Delta$  (not shown here) were measured at different angles to improve the accuracy of the fitted model. (b) Real and imaginary part of the permittivity for the TiO2 and TiO2-Au sample deposited at 700 and 300 °C, (c) absorption spectra for methylene blue for different irradiation times with the Au-TiO2 film grown at 500 °C, and (d) normalized absorbance plotted against the irradiation time for the three different films along with the reference MB solution. Inset shows the mechanism of plasmon-induced charge transfer. Electrons near the Au Fermi level are excited to surface plasmon state and get transferred to TiO2 conduction band where the electron-driven hydrogen evolution half-reaction takes place.

absorption spectra has mainly two components: one arises from Au NPs at their resonant wavelength and the other results from coupling between Au NPs seen at longer wavelengths. In addition, results confirm that the binding energy of Au increases with decreasing NP size and incorporation of Au helps to improve the stoichiometry of TiO2. Photodegradation results conclude that the synergistic impact of lowering of the TiO<sub>2</sub> band gap along with the plasmonic absorption of Au NPs plays a significant role in determining the photoactivity of the thin films. This controlled fabrication of TiO2-Au nanocomposite thin films presents new opportunities to fabricate nanoscale metamaterials and control photon-matter interaction at nanoscale, which could find useful applications in photocatalysis and photovoltaic systems.

# **METHODS**

Thin-Film Growth. Au-TiO<sub>2</sub> films were fabricated using a TiO<sub>2</sub>-Au target prepared by the conventional solid-state sintering process in air at 1000 °C for 3 h. Both pure TiO<sub>2</sub> and Au-TiO<sub>2</sub> thin films were deposited on single-crystal STO(001) substrates using a PLD system (with a KrF excimer laser, Lambda Physik Compex Pro 205,  $\lambda = 248$ nm). The laser beam was focused on the target surface at a 45° angle of incidence to obtain an energy density of approximately 3 J/cm<sup>2</sup>. The base pressure of the chamber was  $1 \times 10^{-6}$  Torr or lower before deposition. The Au-TiO2 samples were deposited with the temperature ranging from 300 to 700 °C and a laser frequency of 5 Hz. To avoid oxygen deficiencies in the films and potential oxidation of Au, an intermediate O2 partial pressure of 20 mTorr was maintained during the depositions. The samples were cooled to room temperature under 100 Torr O2 after the deposition.

Structural, Optical, and Surface Characterization. Structural characterization of the samples was carried out using X-ray diffraction (XRD) and transmission electron microscopy (TEM). XRD  $2\theta$  scans were recorded using PANalytical Empyrean 2 with Cu K $\alpha$  radiation, and the TEM/STEM images and selected area electron diffraction (SAED) patterns were acquired using FEI TALOS 200X. The TEM samples were prepared by cutting and manual grinding, followed by dimpling and ion-polishing (precision ion-polishing system (PIPS II)). Optical characterization was carried using a UV-vis-NIR absorption spectrophotometer (PerkinElmer Lambda 1050). The angular-dependent transmission/reflectivity measurements were performed using total automated measurement system. The incident angle was varied from 10 to 60°. Full-wave simulations were carried out using COMSOL Multiphysics 5.3 to fit the optical measurement results. The chemical composition of the TiO2-Au films was investigated using X-ray photoelectron spectroscopy (XPS) system (Kratos Axis Ultra DLD) with monochromatic Al K $\alpha$  radiation (1486.6 eV).

Photocatalytic Activity Measurement. The photocatalytic activity of different samples was evaluated using photodegradation of methylene blue (MB) dye under solar light using a Newport 300 W xenon arc lamp (model 66902) equipped with an AM 1.5G filter with an intensity of 54 mW/cm<sup>2</sup>. The 10 × 5 mm<sup>2</sup> samples were suspended within the quartz cuvettes in an MB solution. After regular intervals, the samples were measured with a UV-vis spectrometer. The peak area was used to estimate the concentration of MB shown in Figure 5d.

Permittivity Measurements. The permittivity of the TiO<sub>2</sub> and Au-TiO2 nanocomposite was evaluated using spectroscopic ellipsometry (JA Woollam RC2). The incident angle was varied from 55 to 75°, with a step size of 10°. The ellipsometer parameters  $\psi$ and  $\Delta$  are related by the equation:  $r_{\rm p}/r_{\rm s}=\tan(\psi)\,{\rm e}^{({\rm i}\Delta)}$ , where  $r_{\rm p}$  and  $r_{\rm s}$  are the reflection coefficient for the p-polarization and s-polarization light, respectively. The parameters  $\psi$  and  $\Delta$  were fitted using an appropriate model to calculate the dielectric permittivity. The  $\psi$  and  $\Delta$  are measured at different angles to improve the accuracy of the fitted model. The calculations were carried out using the ellipsometry software CompleteEASE. A Cauchy model was used to fit the anatase TiO2. A general oscillator layer consisting of one Tauc-Lorentz oscillator and one Lorentz oscillator was used to fit the Au-TiO2 nanocomposite. The fitted models are shown in Figure S7.

## ASSOCIATED CONTENT

## Supporting Information

The Supporting Information is available free of charge on the ACS Publications website at DOI: 10.1021/acsami.8b12210.

STEM image of Au-TiO2 nanocomposite on MgO(001) substrate, diffraction pattern, X-ray diffraction of Au-TiO2 nanocomposite films, rocking curve, angular dependence measurement, experimental and fitted components of the ellipsometric parameter  $\psi$ (PDF)

## AUTHOR INFORMATION

## **Corresponding Author**

\*E-mail: hwang00@purdue.edu.

ORCID ®

Leigang Li: 0000-0001-6026-4401 Haiyan Wang: 0000-0002-7397-1209

The authors declare no competing financial interest.

## ACKNOWLEDGMENTS

The work was partially supported by the College of Engineering Start-up Fund and Basil R. Turner Professorship at Purdue University. The TEM/STEM imaging effort was funded by the U.S. National Science Foundation (DMR-1565822). S.M. and H.W. acknowledge the support from the U.S. National Science Foundation (DMR-1809520). The authors would like to thank Scott McClary (Purdue University), Prof. Rakesh Agrawal (Purdue University), and Prof. Seungho Cho (Ulsan National Institute of Science and Technology) for help with the photodegradation experiments.

## REFERENCES

- (1) Fujishima, A.; Honda, K. Electrochemical Photolysis of Water at a Semiconductor Electrode. Nature 1972, 238, 37-38.
- (2) Khan, S. U. M.; Al-Shahry, M.; Ingler, W. B., Jr. Efficient Photochemical Water Splitting by a Chemically Modified N-TiO2. Science 2002, 297, 2243-2245.
- (3) Mills, A.; Davies, R. H.; Worsley, D. Water Purification by Semiconductor Photocatalysis. Chem. Soc. Rev. 1993, 22, 417.
- (4) Bach, U.; Lupo, D.; Comte, P.; Moser, J. E.; Weissörtel, F.; Salbeck, J.; Spreitzer, H.; Grätzel, M. Solid-State Dye-Sensitized Mesoporous TiO2 Solar Cells with High Photon-to-Electron Conversion Efficiencies. Nature 1998, 395, 583-585.
- (5) Zhang, Y.; Tang, Z.-R.; Fu, X.; Xu, Y.-J. TiO 2-Graphene Nanocomposites for Gas-Phase Photocatalytic Degradation of Volatile Aromatic Pollutant: Is TiO2-Graphene Truly Different from Other TiO2-Carbon Composite Materials? ACS Nano 2010, 4, 7303-7314.
- (6) Tian, J.; Sang, Y.; Yu, G.; Jiang, H.; Mu, X.; Liu, H. A Bi2WO6-Based Hybrid Photocatalyst with Broad Spectrum Photocatalytic Properties under UV, Visible, and near-Infrared Irradiation. Adv. Mater. 2013, 25, 5075-5080.

- (7) Nishijima, Y.; Ueno, K.; Yokota, Y.; Murakoshi, K.; Misawa, H. Plasmon-Assisted Photocurrent Generation from Visible to Near-Infrared Wavelength Using a Au-Nanorods/TiO2 Electrode. J. Phys. Chem. Lett. 2010, 1, 2031-2036.
- (8) Zhang, Z.; Zhang, L.; Hedhili, M. N.; Zhang, H.; Wang, P. Plasmonic Gold Nanocrystals Coupled with Photonic Crystal Seamlessly on TiO2 Nanotube Photoelectrodes for Efficient Visible Light Photoelectrochemical Water Splitting. Nano Lett. 2013, 13, 14-
- (9) Seh, Z. W.; Liu, S.; Low, M.; Zhang, S.; Liu, Z.; et al. Janus Au-TiO2 Photocatalysts with Strong Localization of Plasmonic Near-Fields for Efficient Visible-Light Hydrogen Generation. Adv. Mater. 2012, 24, 2310-2314.
- (10) Xu, Z.; Lin, Y.; Yin, M.; Zhang, H.; Cheng, C.; Lu, L.; Xue, X.; Fan, H. J.; Chen, X.; Li, D. Understanding the Enhancement Mechanisms of Surface Plasmon-Mediated Photoelectrochemical Electrodes: A Case Study on Au Nanoparticle Decorated TiO2 Nanotubes. Adv. Mater. Interfaces 2015, 2, No. 1500169.
- (11) Shi, H.; Wang, X.; Zheng, M.; Wu, X.; Chen, Y.; Yang, Z.; et al. Hot-Electrons Mediated Efficient Visible-Light Photocatalysis of Hierarchical Black Au-TiO2 Nanorod Arrays on Flexible Substrate. Adv. Mater. Interfaces 2016, 3, No. 1600588.
- (12) Atwater, H. A.; Polman, A. Plasmonics for Improved Photovoltaic Devices. Nat. Mater. 2010, 9, 205-213.
- (13) Linic, S.; Christopher, P.; Ingram, D. B. Plasmonic-Metal Nanostructures for Efficient Conversion of Solar to Chemical Energy. Nat. Mater. 2011, 10, 911-921.
- (14) Kuzyk, A.; Schreiber, R.; Zhang, H.; Govorov, A. O.; Liedl, T.; Liu, N. Reconfigurable 3D Plasmonic Metamolecules. Nat. Mater. 2014, 13, 862-866.
- (15) Cai, W.; Chettiar, U. K.; Kildishev, A. V.; Shalaev, V. M. Optical Cloaking with Metamaterials. Nat. Photonics 2007, 1, 224-227.
- (16) Chang, D. E.; Sorensen, A. S.; Hemmer, P. R.; Lukin, M. D. Quantum Optics with Surface Plasmons. Phys. Rev. Lett. 2006, 97, No. 053002.
- (17) Neumann, O.; Neumann, A. D.; Silva, E.; Ayala-Orozco, C.; Tian, S.; Nordlander, P.; Halas, N. J. Nanoparticle-Mediated, Light-Induced Phase Separations. Nano Lett. 2015, 15, 7880-7885.
- (18) Zhou, L.; Tan, Y.; Wang, J.; Xu, W.; Yuan, Y.; Cai, W.; Zhu, S.; Zhu, J. 3D Self-Assembly of Aluminium Nanoparticles for Plasmon-Enhanced Solar Desalination. Nat. Photonics 2016, 10, 393-398.
- (19) Rycenga, M.; Cobley, C. M.; Zeng, J.; Li, W.; Moran, C. H.; Zhang, Q.; Qin, D.; Xia, Y. Controlling the Synthesis and Assembly of Silver Nanostructures for Plasmonic Applications. Chem. Rev. 2011,
- (20) Mubeen, S.; Hernandez-sosa, G.; Moses, D.; Lee, J.; Moskovits, M. Plasmonic Photosensitization of a Wide Band Gap Semiconductor: Converting Plasmons to Charge Carriers. Nano Lett. 2011, 11, 5548-5552.
- (21) Ratchford, D. C.; Dunkelberger, A. D.; Vurgaftman, I.; Owrutsky, C.; Pehrsson, P. E. Quantification of Efficient Plasmonic Hot-Electron Injection in Gold Nanoparticle-TiO2 Films. Nano Lett. 2017, 6047-6055.
- (22) Subramanian, V.; Wolf, E. E.; Kamat, P. V. Influence of Metal / Metal Ion Concentration on the Photocatalytic Activity of TiO2-Au Composite Nanoparticles. Langmuir 2003, 469-474.
- (23) Tanaka, A.; Ogino, A.; Iwaki, M.; Hashimoto, K.; Ohnuma, A.; Amano, F.; Ohtani, B.; Kominami, H. Gold-Titanium (IV) Oxide Plasmonic Photocatalysts Prepared by a Colloid-Photodeposition Method: Correlation Between Physical Properties and Photocatalytic Activities. Langmuir 2012, 28, 13105-13111.
- (24) Tang, H.; Su, Y.; Zhang, B.; Lee, A. F.; Isaacs, M. A.; Wilson, K.; Li, L.; Ren, Y.; Huang, J.; Haruta, M.; Qiao, B.; Liu, X.; Jin, C.; Su, D.; Wang, J.; Zhang, T. Classical Strong Metal - Support Interactions between Gold Nanoparticles and Titanium Dioxide. Sci. Adv. 2017, No. e1700231.
- (25) Su, Q.; Zhang, W.; Lu, P.; Fang, S.; Khatkhatay, F.; Jian, J.; Li, L.; Chen, F.; Zhang, X.; MacManus-Driscoll, J. L.; Chen, A.; Jia, Q.; Wang, H. Self-Assembled Magnetic Metallic Nanopillars in Ceramic

- Matrix with Anisotropic Magnetic and Electrical Transport Properties. *ACS Appl. Mater. Interfaces* **2016**, *8*, 20283–20291.
- (26) Li, L.; Sun, L.; Gomez-Diaz, J. S.; Hogan, N. L.; Lu, P.; Khatkhatay, F.; Zhang, W.; Jian, J.; Huang, J.; Su, Q.; Fan, M.; Jacob, C.; Li, J.; Zhang, X.; Jia, Q.; Sheldon, M.; Alu, A.; Li, X.; Wang, H. Self-Assembled Epitaxial Au-Oxide Vertically Aligned Nanocomposites for Nanoscale Metamaterials. *Nano Lett.* **2016**, *16*, 3936–3943.
- (27) Huang, J.; Li, L.; Lu, P.; Qi, Z.; Sun, X.; Zhang, X.; Wang, H. Self-Assembled Co–BaZrO3 Nanocomposite Thin Films with Ultra-Fine Vertically Aligned Co Nanopillars. *Nanoscale* **2017**, *9*, 7970–7976.
- (28) Zhang, W.; Ramesh, R.; MacManus-Driscoll, J. L.; Wang, H. Multifunctional, Self-Assembled Oxide Nanocomposite Thin Films and Devices. MRS Bull. 2015, 40, 736–745.
- (29) Huang, J.; Macmanus-driscoll, J. L.; Wang, H. New Epitaxy Paradigm in Epitaxial Self-Assembled Oxide Vertically Aligned Nanocomposite Thin Films. *J. Mater. Res.* **2017**, 32, 4054–4066.
- (30) Chen, A.; Bi, Z.; Jia, Q.; Macmanus-Driscoll, J. L.; Wang, H. Microstructure, Vertical Strain Control and Tunable Functionalities in Self-Assembled, Vertically Aligned Nanocomposite Thin Films. *Acta Mater.* **2013**, *61*, 2783–2792.
- (31) Luttrell, T.; Halpegamage, S.; Tao, J.; Kramer, A.; Sutter, E.; Batzill, M. Why Is Anatase a Better Photocatalyst than Rutile? Model Studies on Epitaxial TiO2 Films. *Sci. Rep.* **2014**, *4*, No. 4043.
- (32) Yoshida, T.; Watanabe, T.; Kikuchi, F.; Tabuchi, T.; Umezu, I.; Haraguchi, M. Pulsed-Laser-Deposited TiO2 Nanocrystalline Films Supporting Au Nanoparticles for Visible-Light-Operating Plasmonic Photocatalysts. *Appl. Phys. A* **2016**, *122*, No. 510.
- (33) Duta, L.; Popescu, C.; Popescu, A.; Motoc, M.; Logofatu, C.; Enesca, A.; Duta, A.; Gyorgy, E. Nitrogen-Doped and Gold-Loaded TiO2 Photocatalysts Synthesized by Sequential Reactive Pulsed Laser Deposition. *Appl. Phys. A: Mater. Sci. Process.* **2014**, *117*, 97–101.
- (34) Walther, T. A New Experimental Procedure to Quantify Annular Dark Field Images in Scanning Transmission Electron Microscopy. *J. Microsc.* **2006**, 221, 137–144.
- (35) Gorbenko, O. Y.; Samoilenkov, S. V.; Graboy, I. E.; Kaul, A. R. Epitaxial Stabilization of Oxides in Thin Films. *Chem. Mater.* **2002**, *14*, 4026–4043.
- (36) Wu, X. L.; Siu, G. G.; Fu, C. L.; Ong, H. C. Photoluminescence and Cathodoluminescence Studies of Stoichiometric and Oxygen-Deficient ZnO Films. *Appl. Phys. Lett.* **2001**, *78*, 2285–2287.
- (37) Fishman, Z. S.; Rudshteyn, B.; He, Y.; Liu, B.; Chaudhuri, S.; Askerka, M.; Haller, G. L.; Batista, V. S.; Pfe, L. D. Fundamental Role of Oxygen Stoichiometry in Controlling the Band Gap and Reactivity of Cupric Oxide Nanosheets. *J. Am. Chem. Soc.* **2016**, *138*, 10978–10985.
- (38) O'Reilly, E. P. Valence Band Engineering in Strained-Layer Structures. Semicond. Sci. Technol. 1989, 4, 121-137.
- (39) Ali, A.; Ruzybayev, I.; Yassitepe, E.; Karim, A.; Shah, S. I.; Bhatti, A. S. Phase Transformations in the Pulsed Laser Deposition Grown TiO 2 Thin Films as a Consequence of O 2 Partial Pressure and Nd Doping. *J. Phys. Chem. C* **2015**, *119*, 11578–11587.
- (40) Tian, Y.; Tatsuma, T. Mechanisms and Applications of Plasmon-Induced Charge Separation at TiO 2 Films Loaded with Gold Nanoparticles. *J. Am. Chem. Soc.* **2005**, *127*, 7632–7637.
- (41) Furube, A.; Du, L.; Hara, K.; Katoh, R.; Tachiya, M. Ultrafast Plasmon-Induced Electron Transfer from Gold Nanodots into TiO 2 Nanoparticles. *J. Am. Chem. Soc.* **2007**, *129*, 14852–14853.
- (42) Stucky, G. D.; Moskovits, M.; Mubeen, S.; Lee, J.; Singh, N.; Kra, S. An Autonomous Photosynthetic Device in Which All Charge Carriers Derive from Surface Plasmons. *Nat. Nanotechnol.* **2013**, *8*, 247–251.
- (43) Murray, W. A.; Barnes, W. L. Plasmonic Materials. *Adv. Mater.* **2007**, *19*, 3771–3782.